Space Sci Rev (2011) 158: 43–68
DOI 10.1007/s11214-011-9751-6

Grad-Shafranov Reconstruction of Magnetic Flux Ropes in the Near-Earth Space

A.T.Y. Lui

Received: 13 May 2010 / Accepted: 18 January 2011 / Published online: 22 April 2011
© Springer Science+Business Media B.V. 2011

Abstract Electric currents permeate space plasmas and often have a significant component along the magnetic field to form magnetic flux ropes. A larger spatial perspective of these structures than from the direct observation along the satellite path is crucial in visualizing their role in plasma dynamics. For magnetic flux ropes that are approximately two-dimensional equilibrium structures on a certain plane, Grad-Shafranov reconstruction technique, developed by Bengt Sonnerup and his colleagues (see Sonnerup et al. in J. Geophys. Res. 111:A09204, 2006), can be used to reveal two-dimensional maps of associated plasma and field parameters. This review gives a brief account of the technique and its application to magnetic flux ropes near the Earth's magnetopause, in the solar wind, and in the magnetotail. From this brief survey, the ranges of the total field-aligned current and the total magnetic flux content for these magnetic flux ropes are assessed. The total field-aligned current is found to range from $\sim$0.14 to $\sim 9.7 \times 10^4$ MA, a range of nearly six orders of magnitude. The total magnetic flux content is found to range from $\sim$0.25 to $\sim 2.3 \times 10^6$ MWb, a range of nearly seven orders of magnitude. To the best of our knowledge, this review reports the largest range of both the total field-aligned current and the total magnetic flux content for magnetic flux ropes in space plasmas.

Keywords Magnetic flux ropes · Grad-Shafranov reconstruction

1 Introduction

Magnetic flux ropes (MFRs) are ubiquitous features in the space environment (Russell and Elphic 1978, 1979; Moldwin and Hughes 1991, 1992; Ieda et al. 1998; Slavin et al. 1998, 2003; Lui et al. 1998, 2007; Linton and Moldwin 2009). These magnetic structures carry field-aligned currents (FACs). Through these FACs, they can exchange energy between plasma regions, e.g., from the magnetosphere to the ionosphere and vice versa. They are

A.T.Y. Lui (✉)
JHU/APL, Laurel, MD 20723-6099, USA
e-mail: Tony.Lui@jhuapl.edu

considered to play an important role in the overall plasma dynamics and coupling between different plasma regions partly because of the link through their FACs.

Although many MFRs have been detected based on measurements from a single spacecraft in the past and present space missions, the inability to extract some intrinsic properties of MFRs, e.g., associated current density, from measurements by a single satellite has hampered our assessment on the role of MFRs in space plasma dynamics. Recently, a useful tool called Grad-Shafranov reconstruction (GSR) has been developed by Bengt Sonnerup and his colleagues to examine MFRs (see Sonnerup et al. 2006 for an overview). The technique is initially employed to analyze data from a single satellite (Sonnerup and Guo 1996; Hau and Sonnerup 1999; Hu and Sonnerup 2001, 2002, 2003; Hu et al. 2004; Teh and Hau 2004, 2007; Du et al. 2007) and is now extended to treat measurements from multiple satellites (Sonnerup et al. 2004; Hasegawa et al. 2005, 2006, 2007; Lui et al. 2008b). It has the ability to extend the vision of the space environment from single point measurements along the satellite path to two-dimensional (2D) maps of plasma and field parameters.

In this review, we show GSR for MFRs in three plasma regions in the near-Earth space. The GSR technique is first briefly described, followed by verification of the method using the four Cluster satellites on a magnetopause crossing event documented by Hasegawa et al. (2004). For additional applications, the MFR observed near the Earth's magnetopause by THEMIS satellites on May 20, 2007 is then analyzed with GSR based on measurements from five satellites. Next, the MFR within an interplanetary coronal mass ejection in the solar wind detected by the ACE satellite on November 20–21, 2003 is analyzed using the GSR technique. This structure was responsible for the occurrence of a superstorm with the minimum Dst reaching −422 nT. Finally, GSR on a MFR observed by the Geotail satellite on January 15, 1994 in the Earth's magnetotail is presented. MFRs in the magnetotail are often found to move tailward, releasing copious amount of mass, momentum, and energy from the near-Earth magnetotail to the distant magnetotail.

2 The Grad-Shafranov Solver and Its Benchmarking

2.1 The Grad-Shafranov Equation

Hau and Sonnerup (1999) discussed in detail the reconstruction of the plasma and field configuration from observation by a single satellite based on solving the Grad-Shafranov (GS) equation. This procedure is applicable to structures having approximately a 2D MHD equilibrium. The GS equation is a second order partial differential equation for the partial vector potential $A(x, y)$:

$$\partial^2 A/\partial x^2 + \partial^2 A/\partial y^2 = -\mu_0 d P_t(A)/dA,$$

where the transverse pressure P_t is defined by $p + B_z^2/2\mu_0$, p is the plasma pressure, μ_0 is the permeability of free space, B_z is the axial magnetic field component perpendicular to the 2D plane on which the GS solution is sought. Let us denote this 2D plane as the GS plane. The magnetic field vector $\mathbf{B}$ is related to the partial vector potential $A(x, y)$ and the axial magnetic field B_z by $\mathbf{B} = \nabla A(x, y) \times \mathbf{z} + B_z(A)\mathbf{z}$. The third dimension represents the direction along which the structure changes much more gradually in comparison to the variations on the GS plane perpendicular to it.

2.2 Procedure in Solving the GS Equation

The GS equation is solved as a spatial initial value problem. The parameters needed are the three components of the magnetic field **B** and the plasma flow **V**, plasma temperature (assumed isotropic), and the plasma mass density. These parameters allow for the computation of the Alfvén speed V_A as well. For completeness, a brief description of the procedure is given below, following that documented in Hau and Sonnerup (1999):

1. A minimum variance analysis (MVA) is performed on **B** to define the variance directions.
2. A deHoffman-Teller (HT) frame transformation (e.g., Khrabrov and Sonnerup 1998) is applied to the observed **B** and **V** to ensure that the structure is in MHD equilibrium in the plasma rest frame. Substantial deviations of the residual velocity from the HT velocity $\mathbf{V}_{\rm HT}$ in comparison to V_A or the sound speed c_s would indicate non-equilibrium of the structure. The MVA and HT results can be used to judge the appropriateness of the steady state 2D assumption of the structure. The term 'steady state' denotes that all parameters associated with the structure do not change in time, including its velocity. This implies that there is no acceleration or net force acting on the structure and it is therefore a static structure.
3. When the above test results conform to the assumption of a convecting 2D structure, one may proceed to define the normal to the GS plane. Let us denote the axes from the MVA by $\mathbf{x}_1$, $\mathbf{x}_2$, and $\mathbf{x}_3$, corresponding to minimum, intermediate, and maximum variance directions. To define the two axes on the GS plane, we make two adjustments. The first is a rotation about the $\mathbf{x}_3$ axis by an angle θ to give the new coordinate system $(\mathbf{x}'_1, \mathbf{x}'_2, \mathbf{x}'_3)$, i.e., $\mathbf{x}'_2 = \mathbf{x}_3, \mathbf{x}'_3 = \mathbf{x}_2 \cos\theta - \mathbf{x}_1 \sin\theta$, $\mathbf{x}'_1 = \mathbf{x}_3 \times \mathbf{x}'_3$. A trial angle θ is used initially. The second is the projection of the deHoffman-Teller velocity onto the $\mathbf{x}'_1\mathbf{x}'_2$ plane, i.e., $\mathbf{V}_{\rm HTt} = (\mathbf{V}_{\rm HT} \bullet \mathbf{x}'_1)\mathbf{x}'_1 - (\mathbf{V}_{\rm HT} \bullet \mathbf{x}'_2)\mathbf{x}'_2$. The final GS coordinate system $(\mathbf{x}''_1, \mathbf{x}''_2, \mathbf{x}''_3)$ is formed with this projection, i.e., $\mathbf{x}''_1 = -\mathbf{V}_{\rm HTt}/|\mathbf{V}_{\rm HTt}|$, $\mathbf{x}''_3 = \mathbf{x}'_3$, $\mathbf{x}''_2 = \mathbf{x}''_3 \times \mathbf{x}''_1$.
4. The time profile of measurements is converted to a spatial profile along the $\mathbf{x}''_1$ axis by $x = |\mathbf{V}_{\rm HTt}|t$.
5. The first step of integration is to obtain $A(x, 0)$ along $\mathbf{x}''_1$ with $A(x, 0) = -\int B_y(x'', 0)\, dx''$, where the lower and upper limits for the integration is 0 and x, respectively.
6. Plot $P_t(x, 0)$ and $B_z(x, 0)$ as a function of $A(x, 0)$. Repeat steps 3 to 5 with a different angle θ to obtain a reasonable presentation, i.e., minimum non-singular values, of P_t and B_z as a function of the partial vector potential $A(x, 0)$. A significant deviation from the optimal orientation for the axis of the approximate 2D structure will reveal itself as non-singular values of $P_t(x, 0)$ as a function of $A(x, 0)$ (Hu and Sonnerup 2002). When a suitable angle θ is determined, then fit $P_t(x, 0)$ and $B_z(x, 0)$ with suitable functions of $A(x, 0)$.
7. The expansion below and above the satellite trajectory is based on the second-order Taylor expansion (Sonnerup and Guo 1996):

$$A(x, y + \Delta y) \approx A(x, y) + (\partial A/\partial y)_{x,y}\Delta y + 0.5(\partial^2 A/\partial y^2)_{x,y}(\Delta y)^2,$$

$$\partial^2 A/\partial y^2 = -\partial^2 A/\partial x^2 - \mu_0 d(p + B_z^2/2\mu_0)/dA,$$

$$(\partial^2 A/\partial x^2)_i = (2A_i - 5A_{i+1} + 4A_{i+2} - A_{i+3})/(\Delta x)^2$$

for forward differentiation at point i,

$$(\partial^2 A/\partial x^2)_i = (A_{i+1} - 2A_i + A_{i-1})/(\Delta x)^2$$

for central point i, and

$$(\partial^2 A/\partial x^2)_i = (2A_i - 5A_{i-1} + 4A_{i-2} - A_{i-3})/(\Delta x)^2$$

for backward differentiation at point i.

Forward differentiation formula is used at the starting boundary points and the backward differentiation formula is used at the ending boundary points.

8. The B_y values are found by $B_y(x, y + \Delta y) = -(\partial A/\partial x)_{x,y+\Delta y}$.
9. The B_x values are obtained from the first order Taylor expansion

$$B_x(x, y + \Delta y) \approx B_x(x, y) + (\partial^2 A/\partial y^2)_{x,y}\Delta y.$$

10. Smoothing is done for the solution of A at each integration step to reduce spurious results.

It is important to note that a precise determination of the optimal axis is not strictly required for GSR. It is more important to ensure that the orientation allows a reasonable fit of the observed parameters. As stated earlier, a significant deviation from the optimal orientation for the axis of the approximate 2D structure will reveal itself as non-singular values of $P_t(x, 0)$ as a function of $A(x, 0)$ (Hu and Sonnerup 2002). Therefore, if an axis can be found such that the variation along that direction is minimum and reasonable fit of the observed parameters can be obtained, then the technique can in principle reconstruct the parameters on a plane perpendicular to the least variability direction. As nature often exhibits variations in many plasma phenomena, it is unlikely that any feature is exactly 2D without any time variation. The usefulness of GSR is its ability to reconstruct an approximate shape and extract properties of the feature outside the satellite path where no observations are available. The GS equation is a Laplacian equation. As noted in Hau and Sonnerup (1999), when such equation is integrated as a Cauchy problem, it is intrinsically unstable and smoothing of the solution at each integration step is needed to suppress spurious numerical errors. Therefore, an exact solution is not expected anyway. The recognition that no GSR solution is an exact one is evidenced by the fact that none of the published work on GSR provides an exact match between GSR solution parameters and observed ones even along the satellite trajectory. The comparison is worse for prediction of parameters at other observation locations.

2.3 Benchmark with a Theoretical Model and IRM Data

For benchmarking of the GS solver, Hau and Sonnerup (1999) and Lui et al. (2008a) have checked the procedure with test cases. The first one is a theoretical model in which the partial magnetic vector potential is given by

$$A(x, y) = \ln\{\alpha \cos(x) + (1 + \alpha^2)^{1/2} \cosh(y)\},$$

where $\alpha = 0.225$, the plasma pressure by $p = e^{-2A}/3\mu_0$, and the axial magnetic field by $B_z = e^{-A}/\sqrt{3}$. For testing, the model structure is rotated by 5.7° with respect to the assumed satellite path. The theoretical (left column) and the numerical (right column) solutions for the six parameters are given in Fig. 1, showing very good match of the numerical solutions with the theoretical ones. Small differences may be noticed at the upper and lower edges of

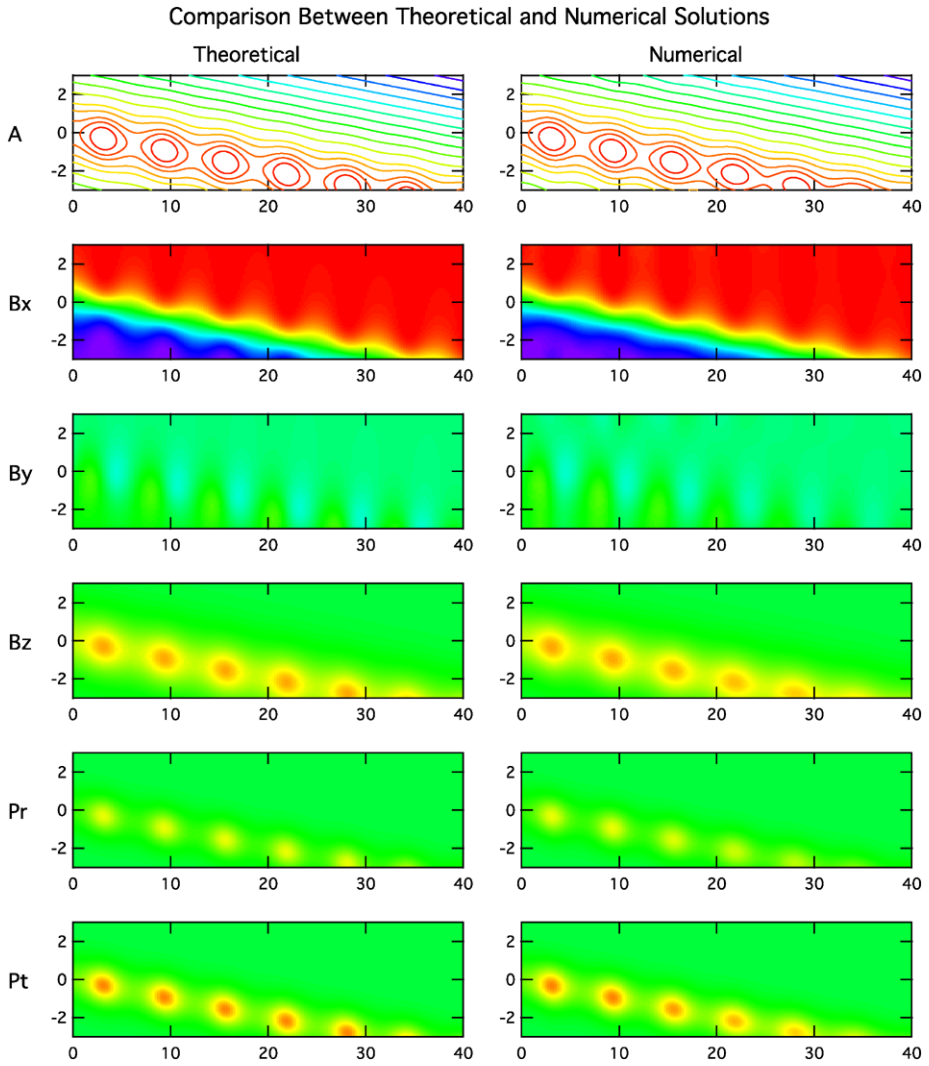

Fig. 1 Benchmarking of the GS solver with a theoretical model: comparison of six plasma parameters between the theoretical (*left column*) and numerical (*right*) solutions (Lui et al. 2008a)

these panels. The error in the numerical solution of $A(x, y)$ in the entire map ranges from -5.3% to 6.0%.

The second test is the IRM event on October 19, 1984, 0517:41–0519:48 UT. The results from the GS solver are shown in Fig. 2, using the optimal angle of $-40°$ chosen by Hau and Sonnerup (1999). The top panel shows the isocontour of $A(x, y)$ along with the magnetic field vectors measured by IRM on the XY-plane. Two pairs of points marked by open circles and crosses are separately on the same isocontour. The middle row shows A along the satellite path and the dependence of P_t on A including the fitted curve. The bottom row shows the variation of p and B_z along the satellite path.

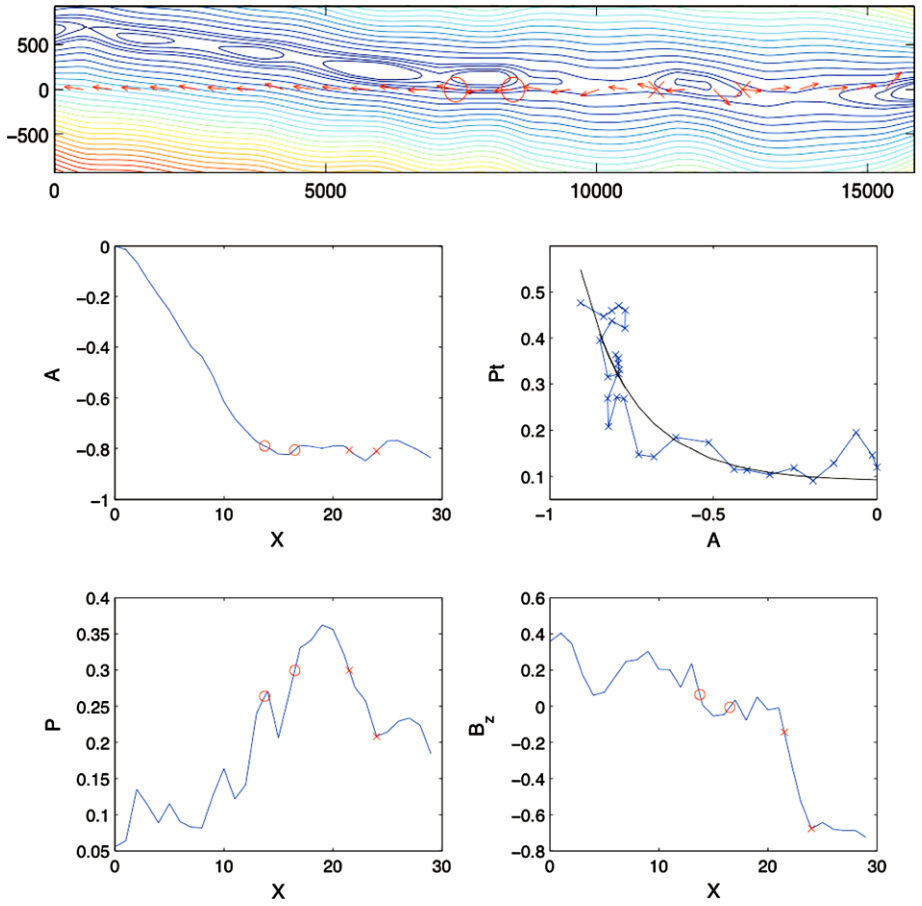

Fig. 2 Benchmarking of the GS solver with an IRM event: isocontour of magnetic vector potential (*top panel*), magnetic vector potential (A) along the satellite path (X), transverse pressure along X, plasma pressure along X, and B_z along X from reconstruction (*bottom four panels*) (Lui et al. 2008a)

3 Verification with Four Cluster Observations

3.1 Cluster Magnetopause Crossing

The verification of the GSR technique is best demonstrated by comparing the predictions of the three components of magnetic field based on one satellite with the observed values from nearby satellites. This verification was performed with Cluster crossing of the magnetopause on June 30, 2001 (Hasegawa et al. 2004). Figure 3 shows the plasma and magnetic field measurements from Cluster on June 30, 2001 around a magnetopause crossing event. Cluster was at $(-7.9, -17.1, 3.3)$ R_E in GSE. It crossed the dawnside magnetopause within the interval 1812–1813 UT. The magnetosheath side had high number density, low temperature, and significant flow speed while the magnetospheric side had low number density, high temperature, and low flow speed (except for C4 which was in the boundary layer). The magnetic field strength was slightly lower on the magnetospheric side.

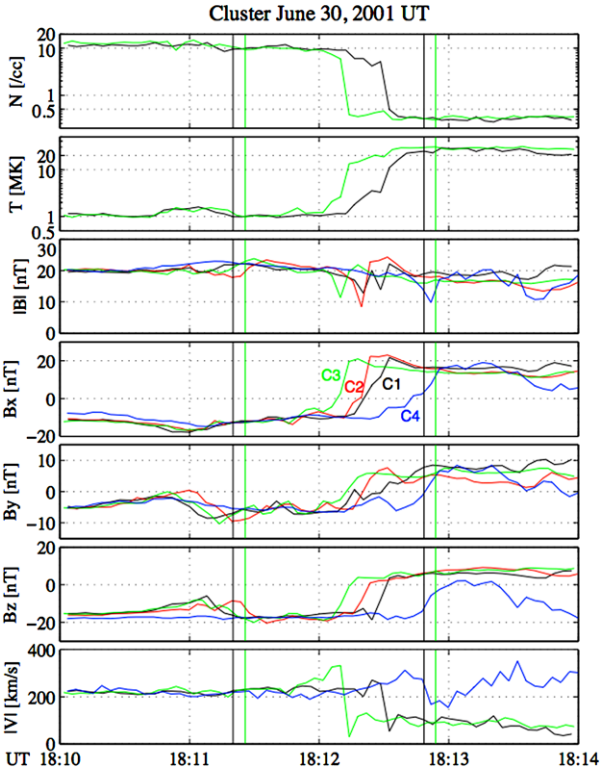

Fig. 3 Cluster measurements during a magnetopause crossing on June 30, 2001. *Panels from top to bottom* show number density, temperature, magnetic field strength and components, and plasma flow speed. Different colors are used to denote different Cluster satellites. The intervals enclosed by the *two black and green vertical lines* are used in the GSR based on C1 and C3 data, respectively (Hasegawa et al. 2004)

3.2 Evaluation on the 2D Equilibrium Condition

For the GSR based on C1 data, the MVA of magnetic field in the interval 1812:00–1812:49 UT yields a magnetopause normal $(0.2003, -0.9654, 0.1671)$ in GSE. The $\mathbf{V}_{\rm HT}$ is determined to be $(-236.6, -83.9, -8.5)$ km/s. The slope for the plot of the residual velocity $|\mathbf{V} - \mathbf{V}_{\rm HT}|$ versus V_A is 0.3430, corresponding to a small field-aligned velocities in the HT frame. These results from MVA and HT analyses are consistent with a 2D equilibrium structure—more details can be found in Hasegawa et al. (2004).

3.3 Reconstruction Results for Cluster

The fitted curves for P_t as a function of A are shown in Fig. 4 for the magnetosheath and the magnetosphere. Based on these fits, 2D maps for B_z and P_t from the GSR are shown in Fig. 5. The reconstructed magnetic field lines are exactly parallel to the projected magnetic field vector at C1 and approximately parallel to those at the other three satellites. The magnetosheath is at the left upper portion of the map where $B_x < 0$ and $B_y < 0$ while the magnetosphere is at the lower right portion where $B_x > 0$ and $B_y > 0$. An X-point is seen at $(x, y) \approx (13500, 0)$ km and links interconnected magnetic field lines with a locally thicker current sheet to its right.

Comparison between the measured magnetic field and the values from GSR for the other three Cluster satellites is shown in Fig. 6 in terms of a time series and in correlation. Different symbols are used for different magnetic field components and different colors denote different satellites. The measured values in solid lines and the GSR values in dashed lines

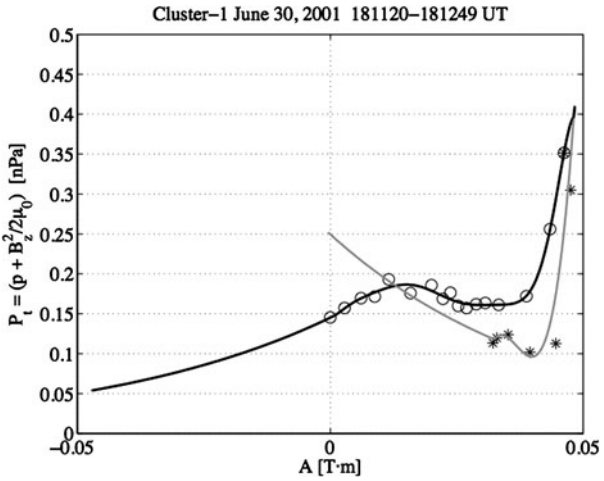

Fig. 4 Plot of transverse pressure versus computed partial vector potential including the fitted curves for the C1 magnetopause crossing data (denoted by *circles* and *stars*). The fitted curves for magnetosheath and magnetosphere are given in *black* and *gray*, respectively (Hasegawa et al. 2004)

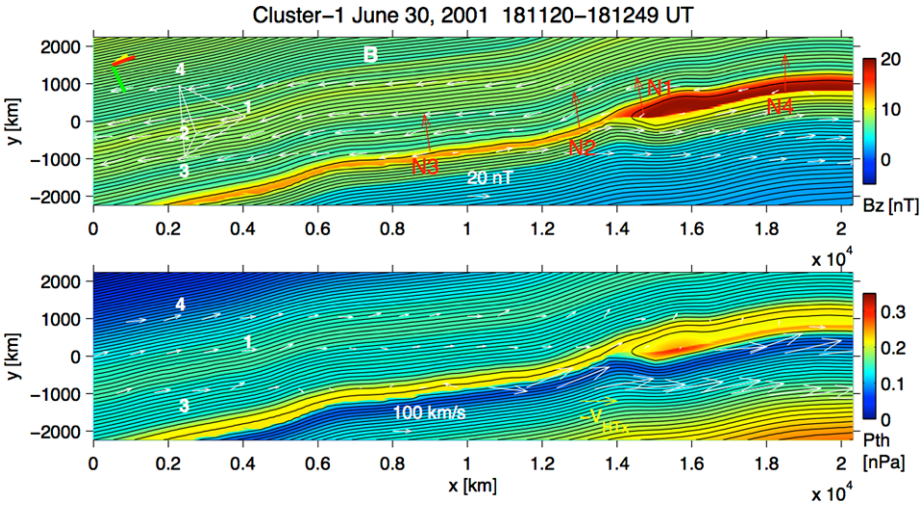

Fig. 5 GSR maps of B_z and P_t. The measured magnetic field vectors are projected on the GS plane as *white arrows* along the satellite trajectories. The *red arrows* denote the vectors normal to the magnetopause from the MVA of the magnetic field (Hasegawa et al. 2004)

compare well for all three satellites with a correlation coefficient of 0.9791. These results provide confidence in the GSR technique.

4 GSR Based on Observations from Five THEMIS Satellites

4.1 THEMIS Magnetopause Crossing

Another verification of the GSR procedure was made by Lui et al. (2008b) for a MFR event observed by the five satellites in the THEMIS (Time History of Events and Macroscale Interactions during Substorms) mission on May 20, 2007 (Sibeck et al. 2008). Figure 7 shows

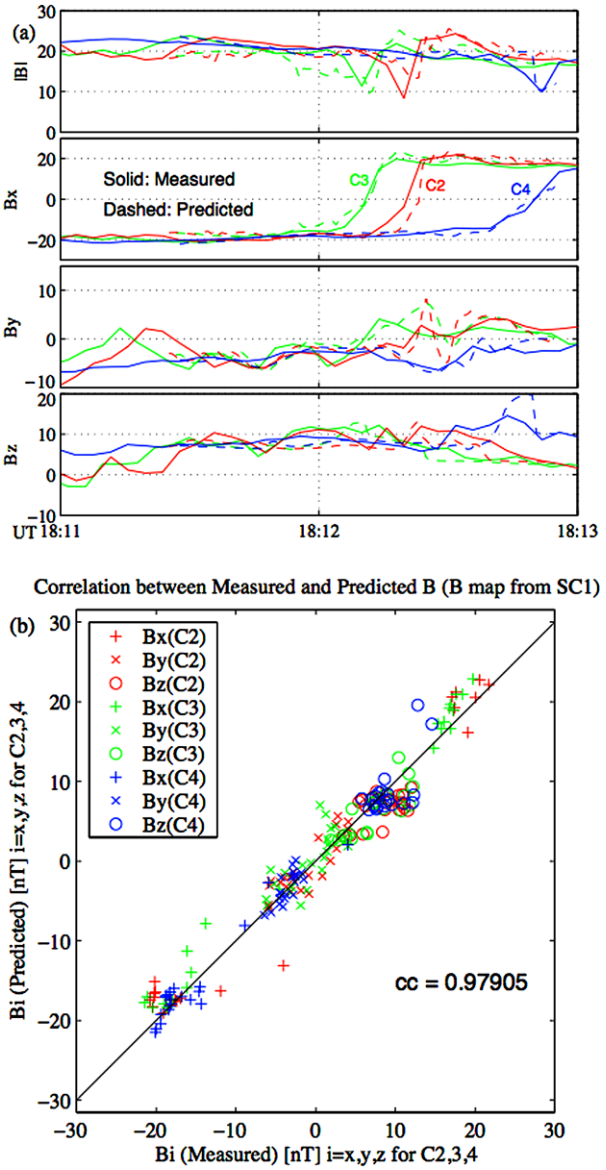

Fig. 6 (**a**) Comparison between the measured magnetic field and that from the GSR; (**b**) A quantitative evaluation on the comparison in (**a**) (Hasegawa et al. 2004)

the plasma and magnetic field measurements for all five THEMIS satellites during 2200–2204 UT. Observations from THEMIS D provide the basis for the GSR since it crossed closest to the core of the MFR. At the start of the interval, THEMIS D was in the magnetosheath, detecting a high plasma density ($\sim$6 cm^{-3}), tailward-duskward plasma flow ($V_x \sim -150$ km/s and $V_y \sim 100$ km/s), and fluctuating southward magnetic field. Observations by the ACE satellite (not shown) indicate that the solar wind had a southward interplanetary magnetic field (IMF) component from $\sim$1900 UT to $\sim$2230 UT at 1 AU. Near the end of the interval, the plasma characteristics at THEMIS D were very different, having a lower plasma density ($\sim$1 cm^{-3}), larger speeds in all flow components, and a relatively

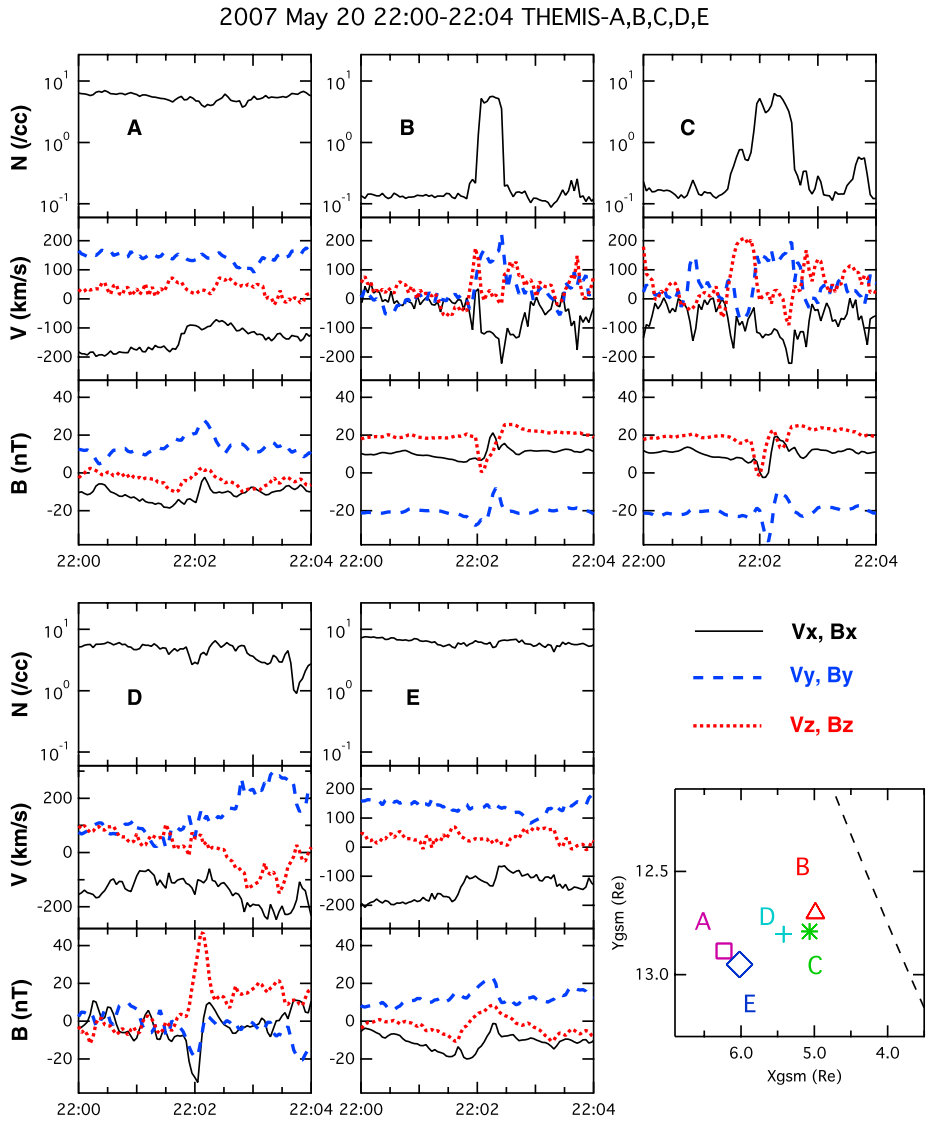

Fig. 7 A brief overview of plasma parameters observed by all five THEMIS satellites for the event on 2007 May 20. The coordinates shown here are GSM. The relative locations of the satellites and their proximities to the nominal magnetopause (*dashed line*) are also shown by the *rightmost panel in the bottom row* of the figure (Lui et al. 2008b)

static northward magnetic field component ($B_z \sim 20$ nT). These are characteristics of a boundary layer. At ~2202 UT within this interval, THEMIS D detected magnetic field characteristics quite distinct from both the adjacent regions. A prominent feature with a strong B_z component was detected for <1 min. A bipolar signature can be seen in both B_x and B_y components in association with the enhancement of the B_z component. These are the expected signatures of a MFR.

THEMIS C was close to THEMIS D and was further into the magnetosphere. It observed mostly plasma with a low number density ($\sim$0.1 cm^{-3}) and was relatively stationary with a high northward magnetic field component ($\sim$20 nT). There is one noticeable difference from the THEMIS D observation. At about the same time when THEMIS D detected the high core magnetic field of a MFR, THEMIS C detected a distinct feature with two depressions in the B_z component. There was an asymmetry in the B_z component, with the B_z minimum deeper before the MFR encounter than afterwards. A bipolar signature was seen in both B_x and B_y components. The core magnetic field strength of the MFR at THEMIS C was noticeably lower than that seen at THEMIS D. This difference in the magnetic field strength indicates that THEMIS C was further away from the core of the MFR than THEMIS D.

Although THEMIS A was immersed well within the magnetosheath during this interval as indicated by the fast tailward-duskward plasma flow and high number density, it observed an enhancement in the B_y component and a reduction of the V_x component at $\sim$2202 UT when the MFR passed over THEMIS D. Similar observations can be seen at THEMIS E, indicating similar effects at THEMIS E when the MFR passed over THEMIS D. There are some similarities and differences between observations from THEMIS B and C. Both were mostly in the magnetosphere sampling a low density and relatively stationary plasma with a strong northward magnetic field. Both encountered significant departures from these plasma characteristics when the MFR passed over THEMIS D. For differences, THEMIS B only saw a single depression in the B_z component and a bipolar signature in the B_y component, but not in the B_x component, when the MFR passed over THEMIS D. This indicates that THEMIS B was even further away from the core of the MFR than THEMIS C.

4.2 Evaluation on the 2D Equilibrium Condition

Since THEMIS D encountered the MFR close to its center, the GS coordinate system for the composite reconstruction is adopted from its reconstruction analysis. The results from MVA are shown in Fig. 8 for the interval 2201:50–2202:20 UT from THEMIS D data. The GSM coordinates of these axes are $B_N = (-0.4522, 0.8331, -0.3186)$, $B_M = (-0.8677, -0.4936, -0.0592)$, and $B_L = (-0.2065, -0.2497, 0.9461)$, with the eigenvalues of 4.364, 177.1, and 243.1, respectively. The MVA result indicates a well-defined B_N axis, implying that it can be represented well as a 2D structure on the plane perpendicular to the B_N axis.

The velocity $V_{\rm HT}$ is found to be $(-91.8, 123.6, -33.6)$ km/s. The correlation coefficient between $-(V \times B)_y$ and $-(V_{\rm HT} \times B)_y$ is 0.969, indicating the existence of a moving frame in which the structure fits well with a relatively steady state condition. The small slope for V–$V_{\rm HT}$ versus V_A (Alfvén velocity) shows a lack of fast flows in the transformed frame, again consistent with the steady state assumption for the structure. These results show that the observed structure has properties satisfying the assumptions for the GSR.

4.3 Reconstruction Results for THEMIS

The angle θ used for the optimal orientation of the axes for GSR is chosen by trial and error to obtain a simple dependence of P_t and B_z on A, which are fitted by a combination of polynomial and exponential functions. This exercise gives $\theta = -75°$. The resulting axes for the reconstruction (using R to denote GSR coordinates) are $XR = (0.5268, -0.7761, 0.3466)$, $YR = (0.7366, 0.6203, 0.2694)$, and $ZR = (-0.4241, 0.1134, 0.8985)$ in GSM coordinates.

Observations from each satellite are then used individually to perform the GSR. Care is needed to combine the separate solutions $A(x, y)$ to cover the entire region because any

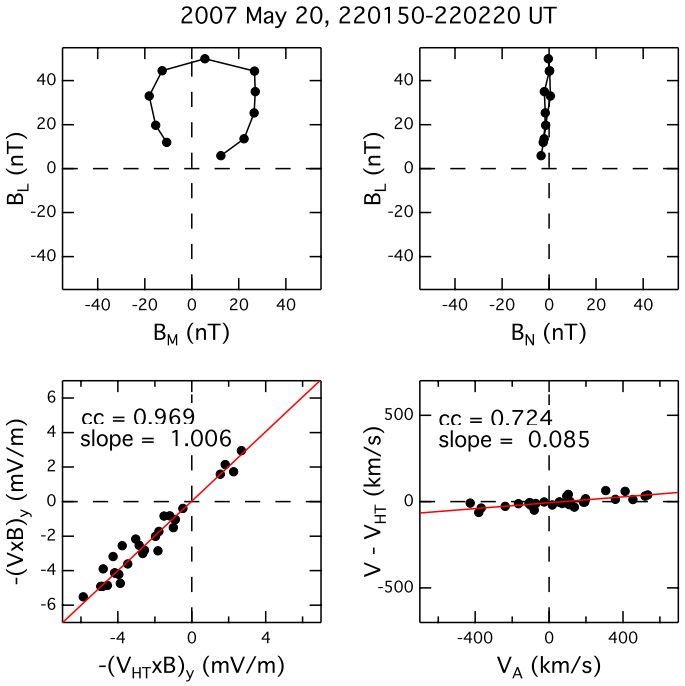

Fig. 8 (**a**) Results from minimum variance analysis, (**b**) results from HT frame transformation (Lui et al. 2008a)

combination of these separate $A(x, y)$, solved with different function of $dP_t(A)/dA$ on the right hand side, does not satisfy the GS equation in general even though the individually derived partial vector potential $A(x, y)$ from each satellite satisfies the GS equation in its region. More precisely, if $A_1(x, y)$ and $A_2(x, y)$ are two different solutions for two different regions associated with $P_{t1}(A_1)$ and $P_{t2}(A_2)$, respectively, i.e.,

$$\partial^2 A_i/\partial x^2 + \partial^2 A_i/\partial y^2 = -\mu_0 dP_{ti}(A_i)/dA_i \quad \text{in region } i = 1, 2,$$

then for $A_c = aA_1 + bA_2$, where a, b are constants as weights to two different solutions,

$$\partial^2 A_c/\partial x^2 + \partial^2 A_c/\partial y^2 = -\mu_0\left[adP_{t1}(A_1)/dA_1 + bdP_{t2}(A_2)/dA_2\right].$$

The right hand side expression cannot in general be expressed as $-\mu_0 dP_{tc}/dA_c$, where $P_{tc} = aP_{t1}(A_1) + bP_{t2}(A_2)$, which is a requirement to satisfy the GS equation for the combined region. In addition, P_{tc} constructed in this way may not be a function of A_c only. The problem becomes worse if $a = a(x, y)$ and $b = b(x, y)$, i.e., they are functions of x and y.

For the above reason, the width of the transition region in producing the partial vector potential $A(x, y)$ for the entire region is minimized by adopting a top-hat function bordered by cosine edges. More specifically, the edge function is given by $f(x) = 0.5 \times [1 + \cos(x/d)\pi]$, where x is the distance from the top-hat edge and d is the width of the edge. This function allows gradual tapering of $A(x, y)$ at the transition boundary between adjacent GS solutions. Also, since an arbitrary constant can be added to $A(x, y)$ without causing any change

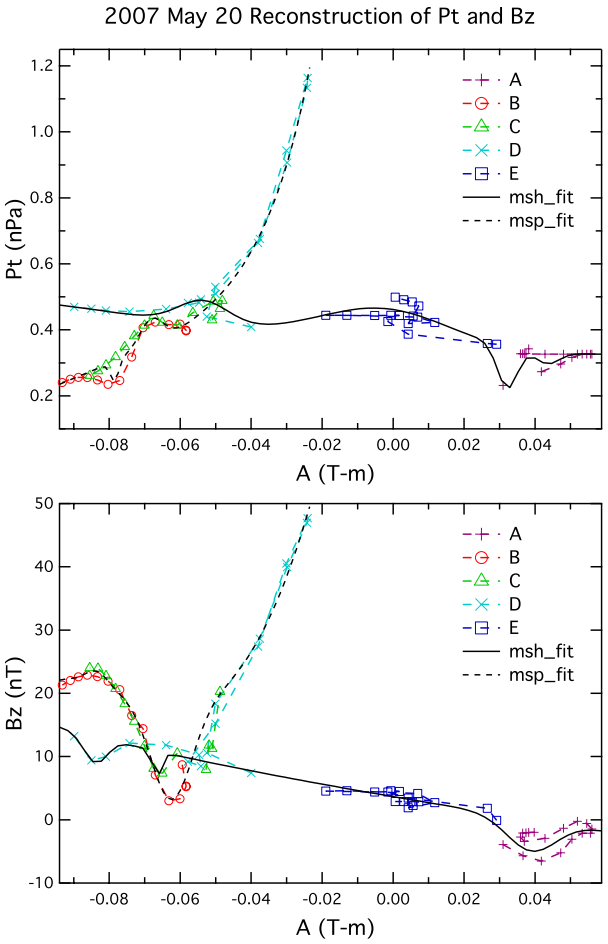

Fig. 9 Plot of P_t and B_z versus computed A for all five THEMIS satellites together with two fitted curves, one for magnetosheath (*solid*) and one for magnetosphere (*dashed*) (Lui et al. 2008b)

in the derived parameters of magnetic field components and plasma pressure, the continuity of $A(x, y)$ at the interfaces of two adjacent reconstruction maps is achieved by adding the average difference of the $A(x, y)$ from the two reconstruction maps at the relevant interface boundary. Note that the above procedure in joining different GS solutions is different from that used by Hasegawa et al. (2005) who adopted a Gaussian function as the weight.

The fitted curves for P_t and B_z as a function of A are shown in Fig. 9. As before, different functions are used for the magnetosheath and the magnetospheric regions. The curves for them are given by solid and dashed lines, respectively. Different colors are used for different satellites. The quantitative comparisons between the observed and GSR values for P_t and B_z for all five THEMIS satellites are shown in Fig. 10. Similarly, different symbols are used for each satellite and different colors are used for each magnetic field component. Note that a slight improvement is made here on the procedure given in Hau and Sonnerup (1999). For the GSR values, although the fitted values of P_r and B_z are used as initial values for integration, the final values along the satellite path on the GS plane are interpolated from the solution values on the two adjacent sides of the satellite path. Therefore, the values of these parameters are indeed obtained from the GS solution and not from the fitted

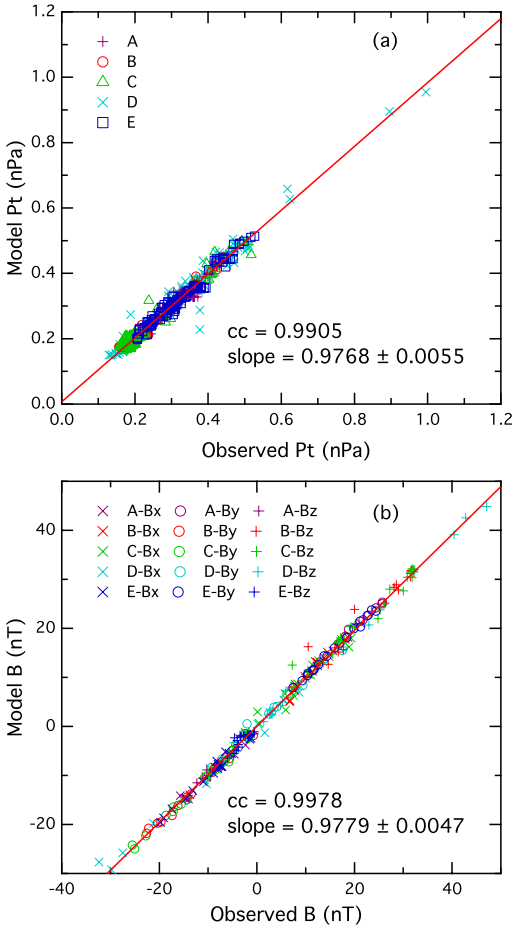

Fig. 10 Comparison between the observed and GSR values for (**a**) the transverse pressure P_t and (**b**) the axial magnetic field component B_z (Lui et al. 2008b)

curves. The good agreement of these parameters from GSR is reflected in the high correlation coefficients for P_t and all magnetic field components, which are 0.9905 and 0.9978, respectively.

Reconstruction 2D maps of transverse and plasma pressures, axial magnetic field, and axial current density are shown in Fig. 11. The axial current density J_z is computed by the Ampere's law with the assumption of a negligible contribution from the displacement current, i.e., $J_z = (\partial B_y/\partial x - \partial B_x/\partial y)/\mu_0$. The horizontal straight lines in these maps indicate paths of the five satellites in the GS XY-plane. Labels of each satellite are given on the right hand side of the reconstruction map for P_t. The MFR appears quite prominently in these construction maps. A noticeable feature is that the parameters shown in these maps show significant differences between the regions above and below the MFR. Also evident in the B_z map is the intrusion of plasma from the magnetosheath region on the right hand side of the map above the MFR at $(X, Y) = (7000, 2000)$ km to the magnetospheric region below the MFR at $(X, Y) = (3000, -2000)$ km. Defining the MFR with $A(x, y) \geq -0.09$ T m, the total magnetic flux contained in this MFR is ~0.25 MWb and the total current within it is ~0.14 MA.

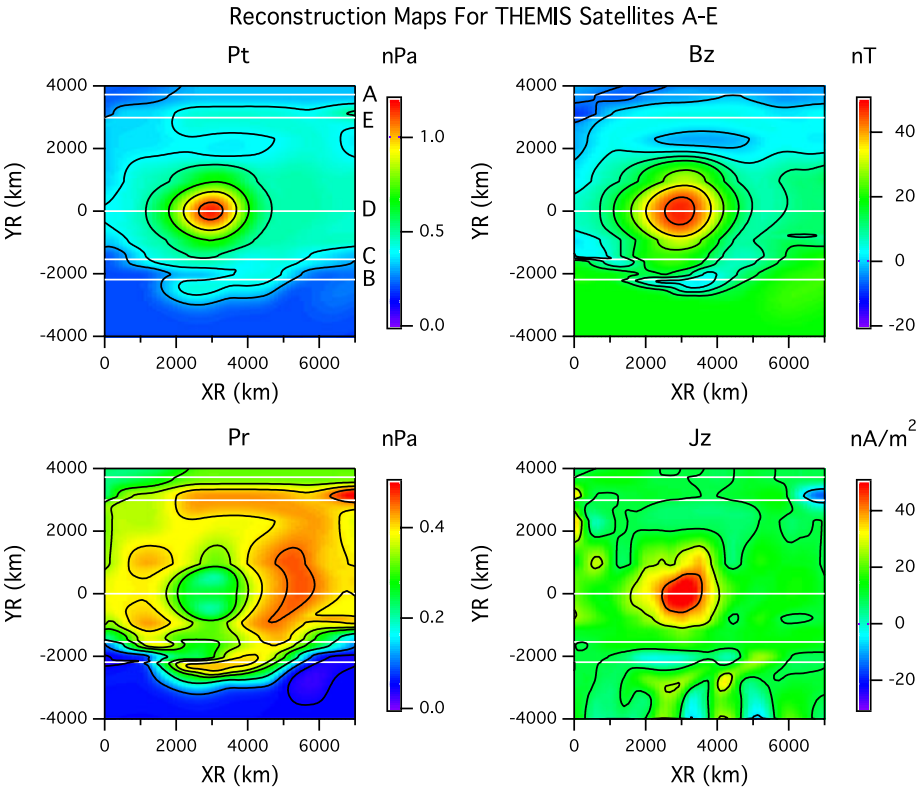

Fig. 11 Composite reconstruction maps of the transverse pressure P_t, the axial magnetic field component B_z, the plasma pressure P_r, and the axial current density B_z based on combined measurements from all five THEMIS satellites (Lui et al. 2008b)

5 GSR for an MFR Linked to a Superstorm

5.1 MFR Linked to a Superstorm on November 20–21, 2003

A superstorm is a geomagnetic storm when its corresponding Dst index reaches below −300 nT (Gonzalez et al. 2001). ACE satellite observed the solar wind features responsible for this superstorm. Figure 12 shows the solar wind parameters and the Dst index. During this interval, signatures of a MFR, also called a magnetic cloud (Burlaga 1995), were seen from ∼1200 UT on November 20, 2003 to ∼0300 UT on November 21, 2003. This MFR had a strong magnetic field, smooth change of magnetic field direction by nearly ∼180°, low proton temperature, and low proton plasma beta.

The solar wind was at the nominal speed of ∼400–450 km/s before the arrival of the MFR and the associated interplanetary shock. The shock front (shown by the vertical dashed line at ∼0800 UT on November 20, 2003) had an initial speed of ∼700 km/s for ∼3 h. After this initial speed jump, the speed gradually decreased down to the pre-shock values by ∼2000 UT on November 21, 2003. The IMF B_z component initially fluctuated between northward and southward for ∼2 h, followed by a sharp rise to ∼34 nT at 1050 UT and descended to negative values at ∼1155 UT on the same day. It remained negative thereafter

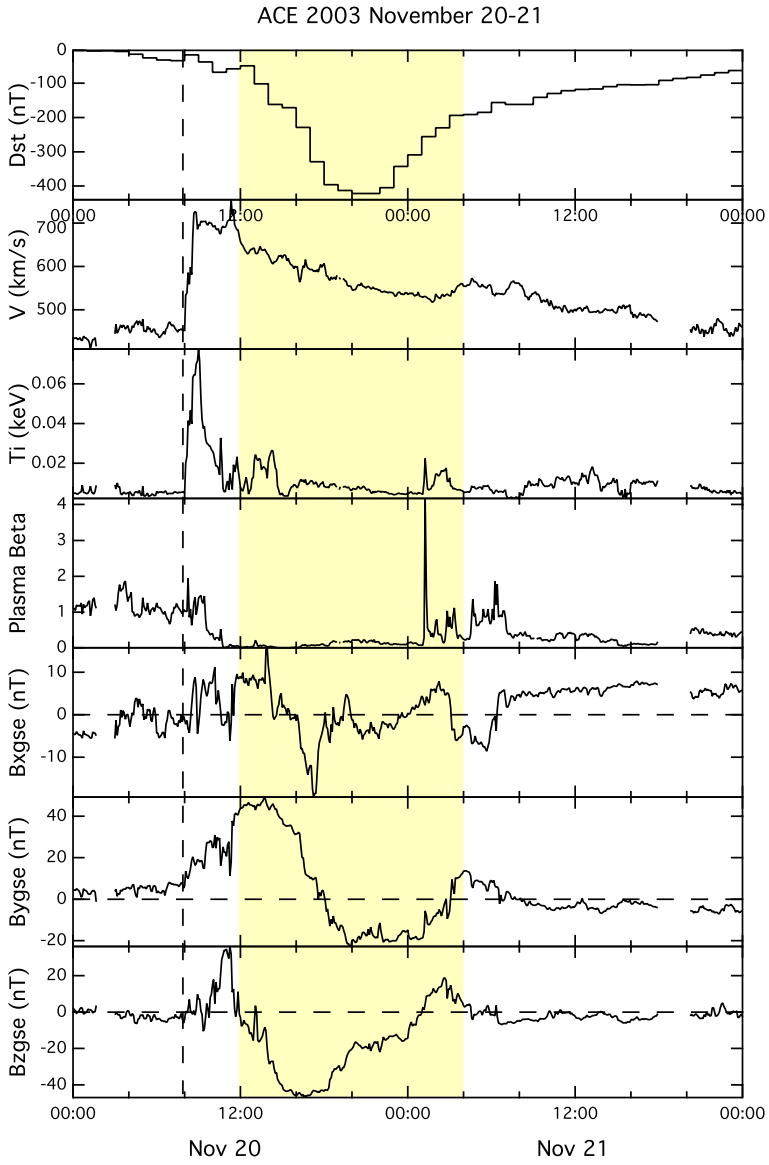

Fig. 12 The *Dst* index and the plasma measurements from the ACE spacecraft during the superstorm of November 20–21, 2003. The three magnetic field components of the solar wind are given in the GSE coordinate system. The ACE data, obtained from OMNI data set in CDAWeb, are time shifted to include the propagation time from the ACE location to the dayside magnetopause. The average time shift for this period is ∼46 min

for ∼14 h with the minimum value of −46 nT. The IMF B_z component reversed to northward at ∼0105 UT on the next day.

The superstorm started slightly before the arrival of the MFR, with Dst reaching −34 nT at 0700 UT on November 20, 2003. The Dst index jumped from −34 nT to −17 nT at the shock arrival. The minimum *Dst* of −422 nT for this superstorm was reached after the sharp

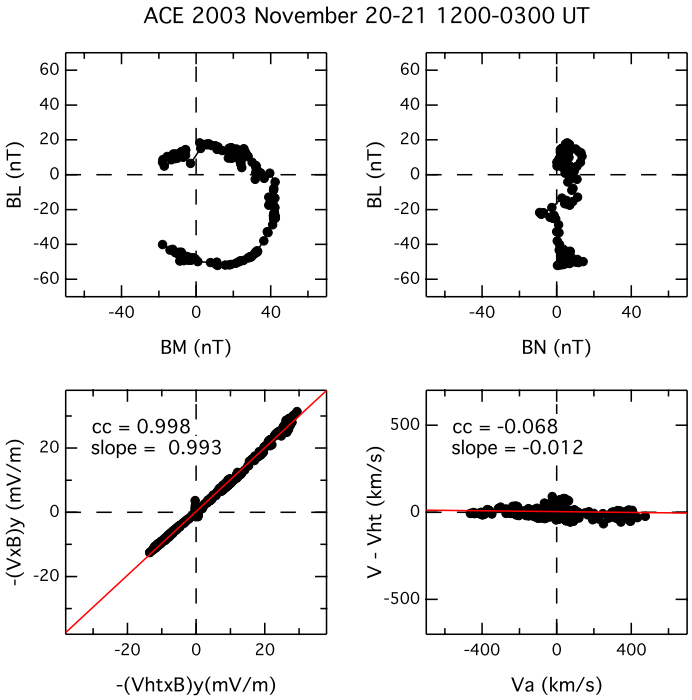

Fig. 13 The results of minimum variance analysis and the deHoffman-Teller frame transformation

minimum in the IMF B_x, the sign reversal of the IMF B_y, and the broad minimum in the IMF B_z.

5.2 Evaluation on the 2D Equilibrium Condition

The interval of interest is shown in Fig. 12 by the highlighted region. For this study, the GSR results are based on 5-min averaged ACE data. The appropriateness of the GSR is verified by performing the MVA and the HT frame transformation, as shown in Fig. 13. The MVA results show the minimum, intermediate, and maximum variances to be $B_N = (0.9596, -0.1307, -0.2492)$, $B_M = (-0.2774, -0.2900, -0.9159)$, $B_L = (-0.0475, -0.9480, 0.3146)$, in GSE coordinates, with the eigenvalues of 12.8, 305.4, and 691.1, respectively, indicating well-defined axes. The V_{HT} velocity is $(-596, 12, -7)$ km/s, with a correlation coefficient of 0.998 between $-(V \times B)_y$ and $-(V_{\mathrm{HT}} \times B)_y$ and a slope of 0.993 ± 0.003. The residual velocity is small in comparison with V_A. These results indicate the existence of a moving frame in which the structure fits well with a relatively steady state condition. Overall, the observed structures have properties satisfying the requirements for the GSR.

The optimal angle for GSR is found to be 62°. The GSR axes are $XR = (0.996, 0.058, -0.067)$, $YR = (-0.006, -0.71, -0.70)$, and $ZR = (-0.088, 0.701, -0.708)$ in GSE coordinates. One may note that the XR-axis is nearly identical to GSE X-axis and the YR-axis is about 45° to both GSE Y-axis and GSE Z-axis.

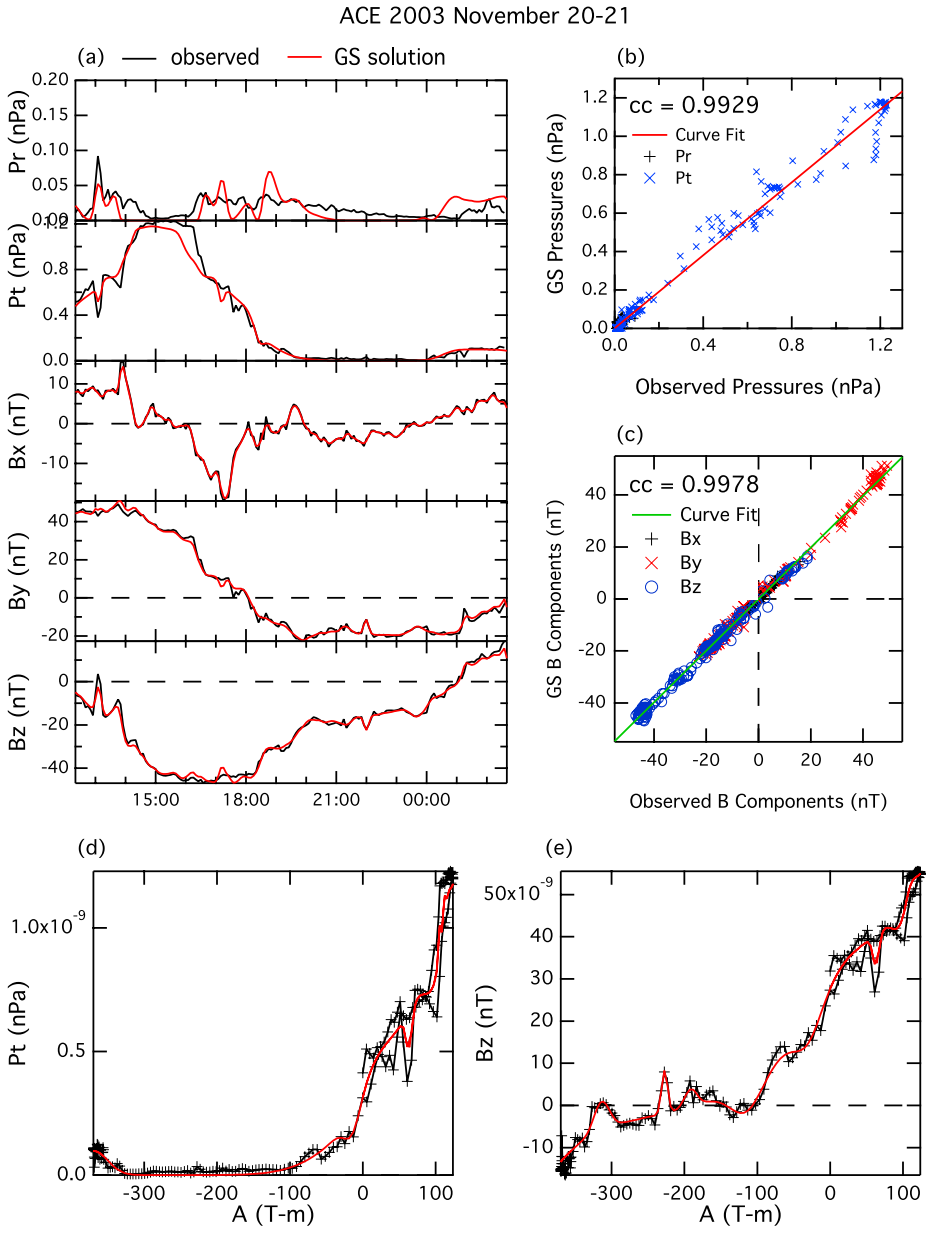

Fig. 14 (**a**) Comparison between the observed and GSR values for the pressure and the magnetic field components; (**b**) a quantitative comparison of pressures between observed and GSR values; (**c**) a quantitative comparison of magnetic field components between observed and GSR values; (**d**) a plot to show the observed P_t as a function of $A(x, y)$ and its fitted curve; (**e**) a plot to show the observed B_z as a function of $A(x, y)$ and its fitted curve

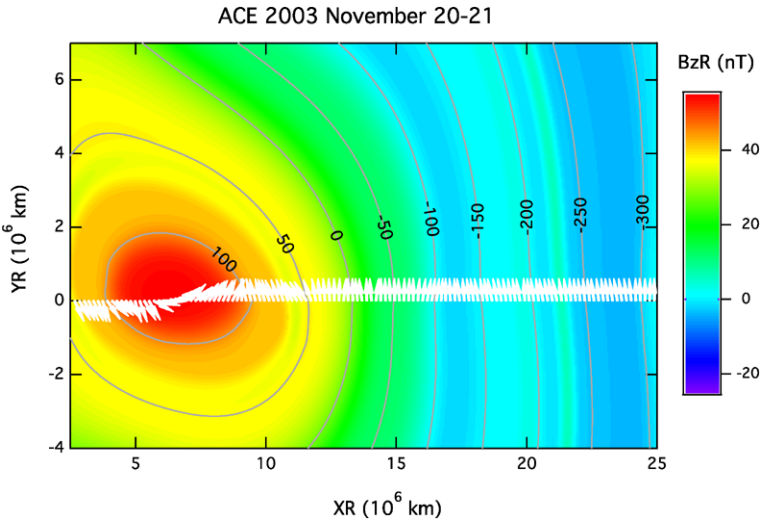

Fig. 15 A 2D map of the B_z component in the GS coordinate system overlaid with contours of $A(x, y)$ and observed normalized magnetic field vectors projected on this GS plane

5.3 Reconstruction Results for the MFR in the Solar Wind

There is good agreement between the observed values of plasma and field parameters with the values from the GSR values (which are not the fitted values as mentioned earlier). Figure 14a shows the time series comparison of these parameters. A quantitative comparison for the transverse and plasma pressures shown in Fig. 14b gives a correlation coefficient of 0.993 and a slope of 0.948 ± 0.006. A quantitative comparison for the magnetic field components shown in Fig. 14c gives the correlation coefficient and the slope to be 0.998 and 0.993 ± 0.003, respectively. The good match is indicated by the correlation coefficient being close to unity. Figures 14d–e show, respectively, the observed P_t and B_z and their fitted curve along the satellite path as a function of $A(x, y)$.

Figure 15 shows the 2D map of the MFR from GSR. The color shows the B_z component in the GS coordinate system and the contours are based on $A(x, y)$ values. The observed normalized magnetic field vectors on this plane are overlaid. It can be seen that the core of the MFR, taken to be the location where B_z was strongest, was at $\sim 78 R_E$ above the satellite path on the YR-axis.

Figure 16 shows the 2D maps of P_t, P_r, and the magnetic field components in GSR coordinates. The transverse pressure P_t had high values ($\sim$1.2 nPa) while P_r had low values ($<$0.1 nPa), indicating that the high values of P_t were mainly contributed by the B_z component. The maximum B_z and B_y in GSR coordinates were $\sim$55 nT and $\sim$59 nT, respectively, within the MFR.

The total magnetic flux content and total field-aligned current within the MFR can be obtained by summing the magnetic flux and current threading through the GS plane. Defining the MFR by $A(x, y) \geq 50$ T m gives the total magnetic flux content to be $\sim 2.3 \times 10^6$ MWb and the total current magnitude to be $\sim 9.7 \times 10^4$ MA. These are probably conservative estimates with the chosen value $A(x, y)$ to define the MFR.

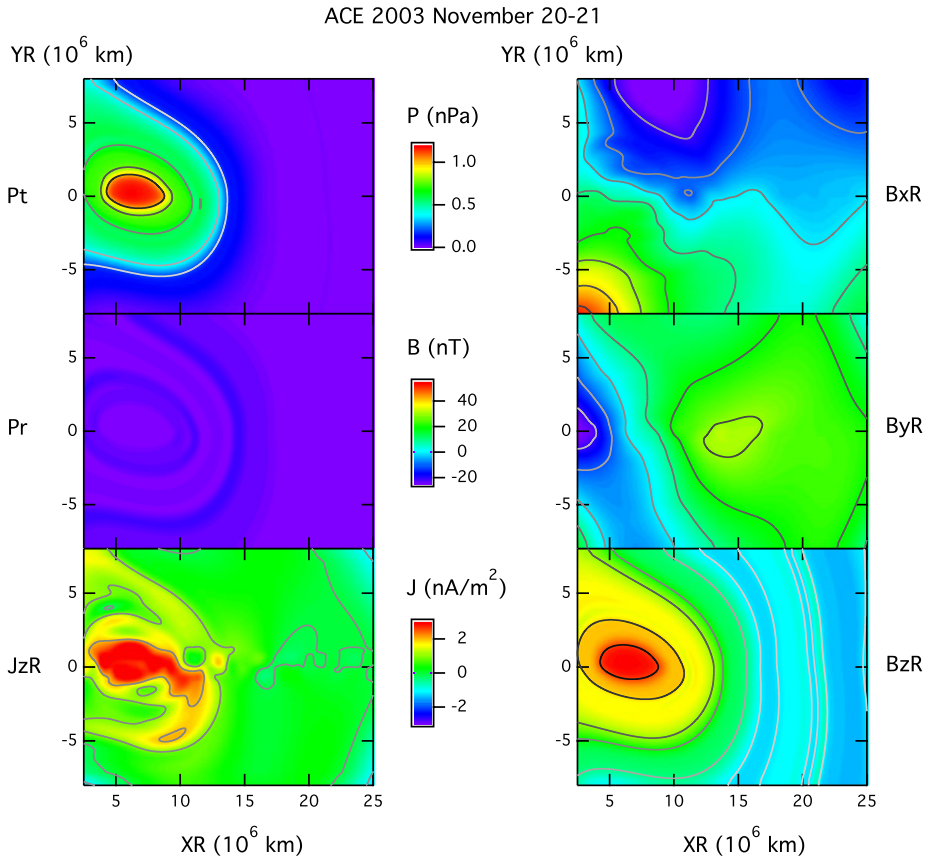

Fig. 16 Two-dimensional maps of the pressures, the axial current density, and the magnetic field components in the GSR coordinate system

6 GSR for MFR in the Magnetotail

6.1 MFR in the Earth's Magnetotail

Figure 17 shows a MFR seen in the magnetotail at the downtail distance of $\sim 96 R_E$. In the early part of the interval, Geotail detected a low-density plasma with a modest sunward flow. It was above the neutral sheet as indicated by the positive B_x component. It soon crossed the neutral sheet multiple times as indicated by the sign reversal in the B_x component. At $\sim$1252 UT, the V_x component reversed in direction to become strongly tailward, at about 1000 km/s at $\sim$1253 UT, and remained so to beyond the end of the interval. Soon after this reversal, a distinct magnetic signature highlighted by the shaded region was detected and lasted for $\sim$6 min. The strength of the B_x and B_z components became very large, accompanied by a bipolar signature in the B_y component. These are the characteristics of a MFR.

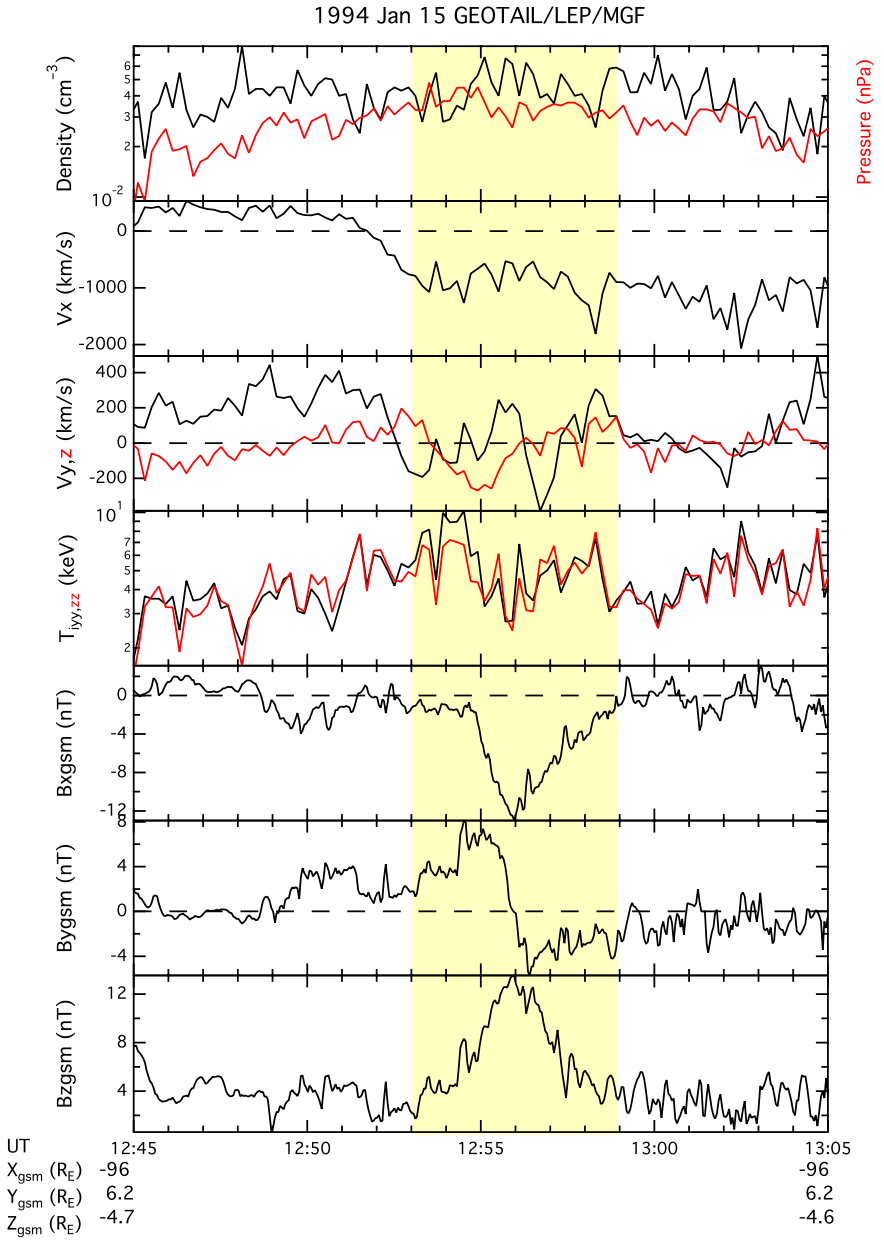

Fig. 17 Plasma parameters of a MFR in the magnetotail measured by Geotail on January 15, 1994

6.2 Evaluation on the 2D Equilibrium Condition

The MFR is analyzed for the appropriateness of the steady state 2D equilibrium assumption. The hodograms from MVA of this MFR are shown in Fig. 18. The MVA results show the minimum, intermediate, and maximum variance axes in the GSM co-

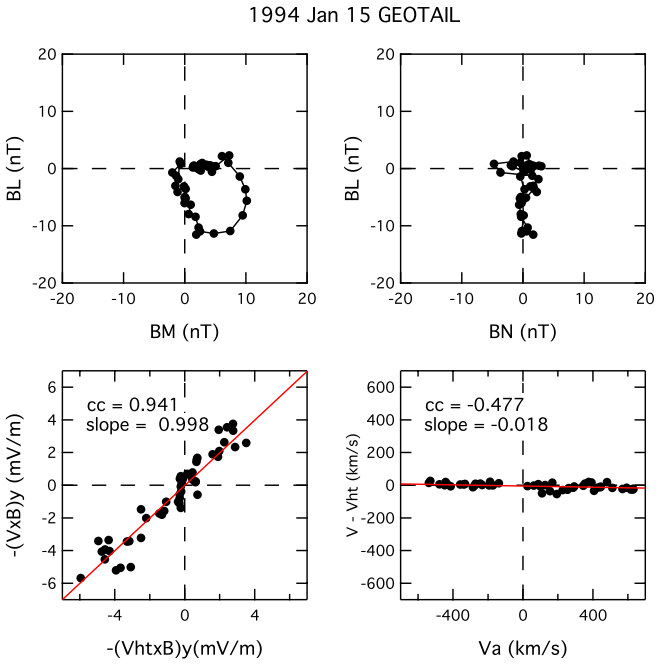

Fig. 18 The results of minimum variance analysis and the deHoffman-Teller frame transformation on the MFR observed by Geotail

ordinates to be $B_N = (-0.2710, 0.7943, 0.5437)$, $B_M = (0.2264, -0.4964, 0.8380)$, and $B_L = (0.9356, 0.3503, -0.0453)$, with eigenvalues of 2.1, 9.3, and 15.8, respectively. The velocity $V_{\rm HT}$ is found to be $(-728.3, -97.7, -9.1)$ km/s. The correlation coefficient between $-(VxB)_y$ and $-(V_{\rm HT}xB)_y$ is 0.941. The slope of -0.018 for $V-V_{\rm HT}$ versus V_A is small, indicating a lack of fast flows in the transformed frame. These results show that the observed structure has properties satisfying the assumptions needed for GS reconstruction.

6.3 Reconstruction Results for the MFR in the Earth's Magnetotail

The optimal angle for GSR is found to be 60°. With this angle, the axes in the GSM coordinates are found to be $XR = (0.9375, 0.3471, 0.0243)$, $YR = (-0.0048, -0.0571, 0.9984)$, and $ZR = (0.3479, -0.9361, -0.0519)$. The time series comparison between the observed and GSR model values for the plasma pressure and the magnetic field components are given in Fig. 19a. One may see that the observed characteristics of this MFR are modeled well by the close match between observed values and GSR model values. These observed characteristics include the strong core field and the bipolar signature of the B_z component. More quantitative comparisons of these quantities are given in Figs. 19b–c. Again, different magnetic field components are shown with different colors and symbols. Linear fits between the observed and model parameters, given by the green lines in these panels, show high correlation coefficients of 0.9881 and 0.9979 for pressure and magnetic field components, respectively. Figures 19d–e show, respectively, the observed P_t and B_z and their fitted curve along the satellite path as a function of $A(x, y)$.

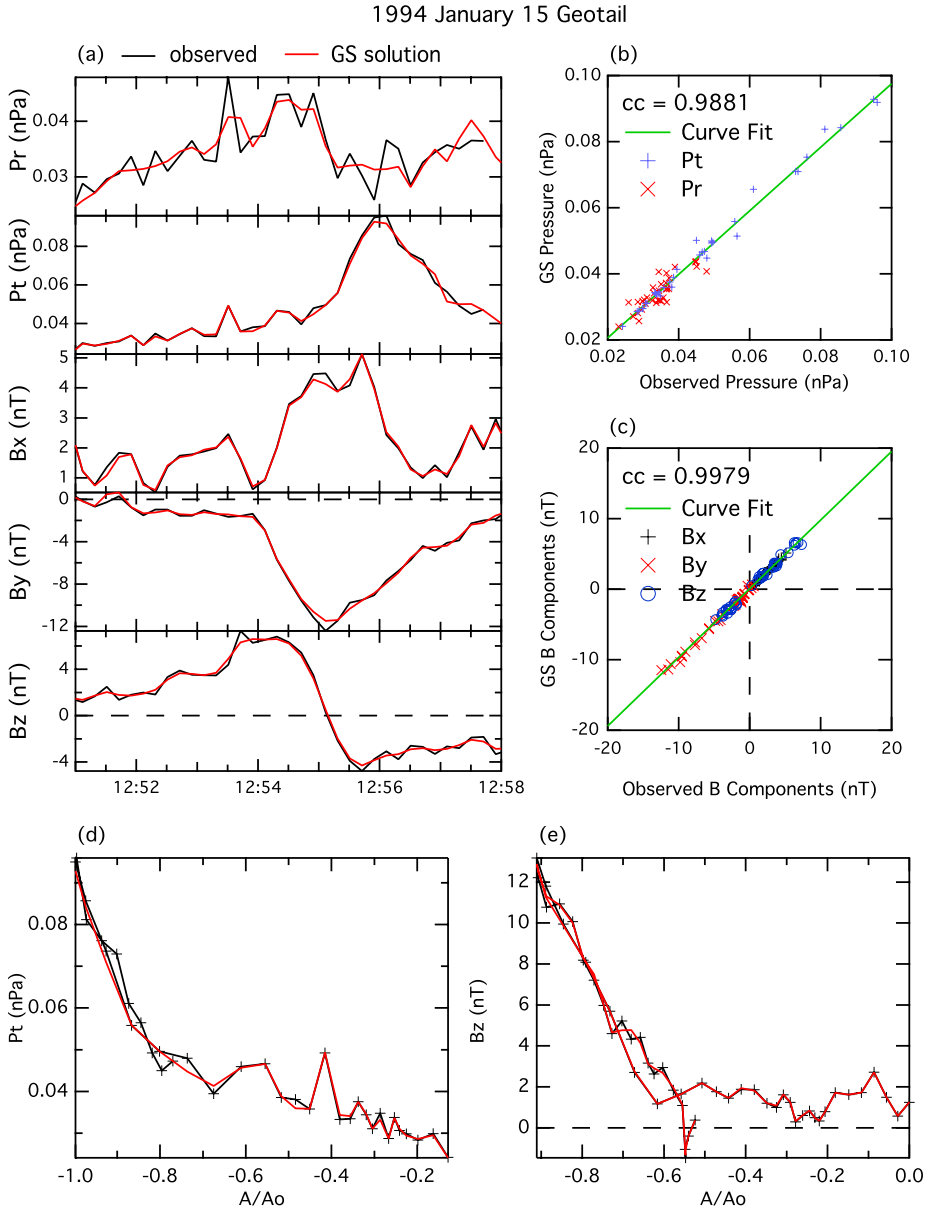

Fig. 19 (**a**) Comparison between the observed and GSR values for the pressure and the magnetic field components; (**b**) a quantitative comparison of pressures between observed and GSR values; (**c**) a quantitative comparison of magnetic field components between observed and GSR values; (**d**) a plot to show the observed P_t as a function of $A(x, y)$ and its fitted curve; (**e**) a plot to show the observed B_z as a function of $A(x, y)$ and its fitted curve

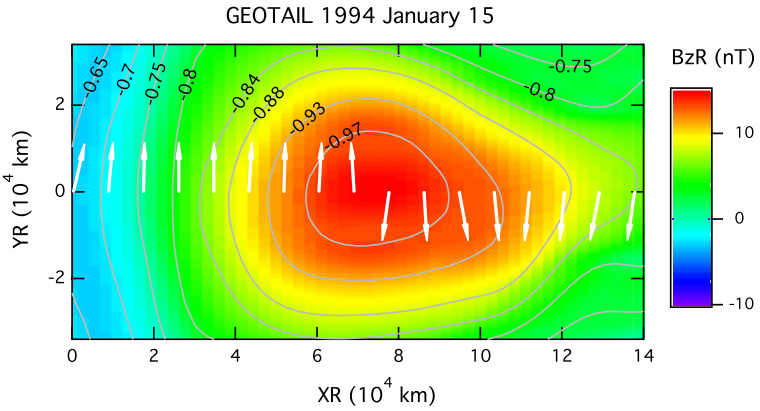

Fig. 20 A 2D map of the B_z component in the GS coordinate system overlaid with contours of $A(x, y)$ and observed normalized magnetic field vectors projected on this GS plane

Figure 20 shows the 2D map of the MFR. The color shows the B_z component in the GS coordinate and the contours are based on $A(x, y)$ values. The observed normalized magnetic field vectors on this plane are overlaid. Geotail crossed very close to the core of the MFR.

The 2D maps of the parameters obtained from the GSR are shown in Fig. 21. In particular, the MFR is indicated in the 2D maps of A, P_t, and B_z by the area of high values of P_t and B_z. Defining the MFR by $A(x, y) \leq -0.84$ T m, the size of the MFR is ~60,000 km × 80,000 km, i.e., a geometric shape slightly elongated in the XR-direction. The axial current density J_z is quite small, about -0.5 nA/m^2, and opposite to the ZR-axis. The total magnetic flux contained in this MFR is ~49 MWb and the total current within it is ~1.4 MA (in the direction opposite to the ZR-axis).

7 Summary

The Grad-Shafranov reconstruction technique used to extend the vision of plasma and field parameters of a magnetic structure from a single satellite path through the structure to two-dimensions is briefly described. This technique, applicable to an approximately two-dimensional equilibrium structure, is then applied to examine magnetic flux ropes in the solar wind, at the Earth's magnetopause, and in the magnetotail. The total field-aligned current and the total magnetic flux content embedded within these structures are assessed through these reconstructions. It is found that the total field-aligned current ranges from ~0.14 to ~9.7×10^4 MA, a range of nearly six orders of magnitude. The total magnetic flux content ranges from ~0.25 to ~2.3×10^6 MWb, a range of nearly seven orders of magnitude. The largest numbers are those found in the interplanetary coronal mass ejection and the lowest ones are those found at the Earth's magnetopause. To the best of our knowledge, this review reports the largest range of both the total field-aligned current and the total magnetic flux content in magnetic flux ropes found in space plasmas. It would be worthwhile to examine many more of these magnetic structures in space plasmas with this technique to gain more insight into their properties and their role in plasma dynamics in different space plasma regions.

Sonnerup et al. (2006) pointed out that the basic Grad-Shafranov reconstruction technique could be extended to other applications. In their review, they have shown three possible extensions: (1) 2D MHD structures with dynamically important field-aligned plasma

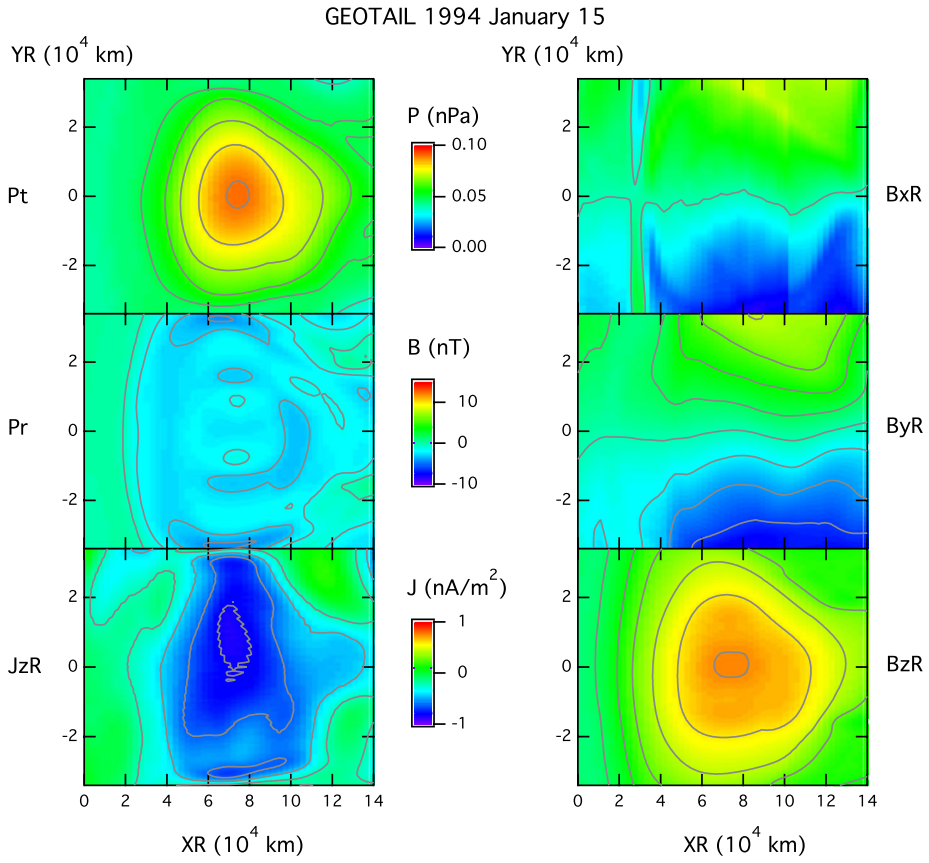

Fig. 21 Two-dimensional maps of the pressures, the axial current density, and the magnetic field components in the GS coordinate system

flows, (2) 2D plasma flow transverse to the magnetic field in the magnetospheric low-latitude boundary layer, and (3) 2D ordinary hydrodynamic flow. Therefore, there is much to be gained by exploring this technique to apply to other space plasma phenomena not discussed here as well as to other scientific disciplines.

Acknowledgements This work was supported by NSF grant ATM-0630912 and NASA grant NNX07AQ-50G to The Johns Hopkins University Applied Physics Laboratory.

References

L.F. Burlaga, *Interplanetary Magnetohydrodynamics* (Oxford University Press, New York, 1995), p. 91

D. Du, C. Wang, Q. Hu, Propagation and evolution of a magnetic cloud from ACE to Ulysses. J. Geophys. Res. **112**, A09101 (2007). doi:10.1029/2007JA012482

W.D. Gonzalez, A.L. Clua-Gonzale, J.H.A. Sobral, A. dal Lago, L.E. Vieira, Solar and interplanetary causes of very intense geomagnetic storms. J. Atmos. Sol.-Terr. Phys. **63**, 403–412 (2001)

H. Hasegawa, B.U.Ö. Sonnerup, M.W. Dunlop, A. Balogh, S.E. Haaland, B. Klecker, G. Paschmann, B. Lavraud, I. Dandouras, H. Rème, Reconstruction of two-dimensional magnetopause structures from Cluster observations: verification of method. Ann. Geophys. **22**, 1251–1266 (2004)

H. Hasegawa, B.U.Ö. Sonnerup, B. Klecker, G. Paschmann, M.W. Dunlop, H. Rème, Optimal reconstruction of magnetopause structures from Cluster data. Ann. Geophys. **23**, 973–982 (2005)
H. Hasegawa, B.U.Ö. Sonnerup, C.J. Owen, B. Klecker, G. Paschmann, A. Balogh, H. Rème, Y. Khotyaintsev, The structure of flux transfer events recovered from Cluster data. Ann. Geophys. **24**, 603–618 (2006)
H. Hasegawa, R. Nakamura, M. Fujimoto, V.A. Sergeev, E.A. Lucek, H. Rème, Y. Khotyaintsev, Reconstruction of a bipolar magnetic signature in an earthward jet in the tail: flux rope or 3D guide-field reconnection? J. Geophys. Res. **112**, A11206 (2007). doi:10.1029/2007JA012492
L.-N. Hau, B.U.Ö. Sonnerup, Two-dimensional coherent structures in the magnetopause: recovery of static equilibria from single-spacecraft data. J. Geophys. Res. **104**, 6899–6917 (1999)
Q. Hu, B.U.Ö. Sonnerup, Reconstruction of magnetic flux ropes in the solar wind. Geophys. Res. Lett. **28**(3), 467–470 (2001)
Q. Hu, B.U.Ö. Sonnerup, Reconstruction of magnetic clouds in the solar wind: orientations and configurations. J. Geophys. Res. **107**, 1142 (2002). doi:10.1029/2001JA000293
Q. Hu, B.U.Ö. Sonnerup, Reconstruction of two-dimensional structures in the magnetopause: method improvements. J. Geophys. Res. **108**, A11011 (2003). doi:10.1029/2002JA009323
Q. Hu, C.W. Smith, N.F. Ness, Double flux-rope magnetic cloud in the solar wind at 1 AU. Geophys. Res. Lett. **30**, 1385 (2004). doi:10.1029/2002GL016653
A. Ieda, S. Machida, T. Mukai, Y. Saito, T. Yamamoto, A. Nishida, T. Terasawa, S. Kokubun, Statistical analysis of the plasmoid evolution with Geotail observations. J. Geophys. Res. **103**, 4453–4465 (1998)
A.V. Khrabrov, B.U.Ö. Sonnerup, DeHoffmann-Teller analysis, in *Analysis Methods for Multi-Spacecraft Data*, ed. by G. Paschmann, P.W. Daly (Int. Space Sci. Inst., Bern, 1998), pp. 221–248, Chap. 9
M.G. Linton, M.B. Moldwin, A comparison of the formation and evolution of magnetic flux ropes in solar coronal mass ejections and magnetotail plasmoids. J. Geophys. Res. **114**, A00B09 (2009). doi:10.1029/2008JA013660
A.T.Y. Lui, D.J. Williams, R.W. McEntire, S.P. Christon, T.E. Eastman, T. Yamamoto, S. Kokubun, Ion composition and charge state of energetic particles in flux ropes/plasmoids. J. Geophys. Res. **103**, 4467–4475 (1998)
A.T.Y. Lui, M.W. Dunlop, H. Rème, L.M. Kistler, G. Gustafsson, Q. Zong, The internal structure of a magnetic flux rope from Cluster observations. Geophys. Res. Lett. **34**, L07102 (2007). doi:10.1029/2007GL029263
A.T.Y. Lui, D.G. Sibeck, T. Phan, V. Angelopoulos, J. McFadden, C. Carlson, D. Larson, J. Bonnell, K.-H. Glassmeier, S. Frey, Reconstruction of a magnetic flux rope from THEMIS observations. Geophys. Res. Lett. **35**, L17S05 (2008a). doi:10.1029/2007GL032933
A.T.Y. Lui, D.G. Sibeck, T. Phan, V. Angelopoulos, J. McFadden, K.-H. Glassmeier, Composite Grad-Shafanov reconstruction of a magnetic flux rope based on observations from five THEMIS satellites. J. Geophys. Res. **113**, A00C01 (2008b). doi:10.1029/2008JA013189
M.B. Moldwin, W.J. Hughes, Plasmoids as magnetic flux ropes. J. Geophys. Res. **96**(A8), 14051–14064 (1991)
M.B. Moldwin, W.J. Hughes, On the formation and evolution of plasmoids: a survey of ISEE 3 Geotail data. J. Geophys. Res. **97**(A12), 19259–19282 (1992)
C.T. Russell, R.C. Elphic, Initial ISEE magnetometer results: magnetopause observations. Space Sci. Rev. **22**, 681–715 (1978)
C.T. Russell, R.C. Elphic, Observation of magnetic flux ropes in the Venus ionosphere. Nature **279**, 616–618 (1979)
D.G. Sibeck, M. Kuznetsova, V. Angelopoulos, K.-H. Glaßmeier, J.P. McFadden, Crater FTEs: simulation results and THEMIS observations. Geophys. Res. Lett. **35**, L17S06 (2008). doi:10.1029/2008GL033568
J.A. Slavin, D.H. Fairfield, M.M. Kuznetsova, C.J. Owen, R.P. Lepping, S. Taguchi, T. Mukai, Y. Saito, T. Yamamoto, S. Kokubun, A.T.Y. Lui, G.D. Reeves, ISTP observations of plasmoid ejection: IMP 8 and Geotail. J. Geophys. Res. **103**, 119–133 (1998)
J.A. Slavin, R.P. Lepping, J. Gjerloev, D.H. Fairfield, M. Hesse, C.J. Owen, M.B. Moldwin, T. Nagai, A. Ieda, T. Mukai, Geotail observations of magnetic flux ropes in the plasma sheet. J. Geophys. Res. **108**(A1), 1015 (2003). doi:10.1029/2002JA009557
B.U.Ö. Sonnerup, M. Guo, Magnetopause transects. Geophys. Res. Lett. **23**, 3679–3682 (1996)
B.U.Ö. Sonnerup, H. Hasegawa, G. Paschmann, Anatomy of a flux transfer event seen by Cluster. Geophys. Res. Lett. **31**, L11803 (2004). doi:10.1029/2004GL020134
B.U.Ö. Sonnerup, H. Hasegawa, W.-L. Teh, L.-N. Hau, Grad-Shafranov reconstruction: an overview. J. Geophys. Res. **111**, A09204 (2006). doi:10.1029/2006JA011717
W.-L. Teh, L.-N. Hau, Evidence for pearl-like magnetic island structures at dawn and dusk side magnetopause. Earth Planets Space **56**, 681–686 (2004)
W.-L. Teh, L.-N. Hau, Triple crossings of a string of magnetic islands at duskside magnetopause encountered by AMPTE/IRM satellite on 8 August 1985. J. Geophys. Res. **112**, A08207 (2007). doi:10.1029/2007JA012294